Machine Learning-Based Wheel Monitoring for Sapphire Wafers

YU-KUN LIN[ID], (Student Member, IEEE), AND BING-FEI WU[ID], (Fellow, IEEE)

Institute of Electrical and Control Engineering, National Chiao Tung University, Hsinchu 300, Taiwan

Corresponding author: Yu-Kun Lin (yukun.lin.ece05g@g2.nctu.edu.tw)

ABSTRACT The thinning of sapphire wafers is a key process that affects the quality of optoelectronic devices. In the grinding process for sapphire, a hard and brittle material, the grade and surface conditions (wearing and chip loading) of the grinding wheel are the key to continuous processing and reduction of defects. In industry, a common approach is to assume the possible causes of defects by observing the spindle current during the grinding process and the finished product after processing. Thus far, there has been no effective method to quantify the grade and no real-time monitoring technology for grinding wheels. This research proposes a wheel monitoring system that utilizes acoustic emission (AE) signals and radial/axial vibration signals to extract characteristic parameters via popular machine learning classification algorithms (k-NN, ANN, and SVM) in order to identify the signal and characteristic parameters of the wheel during the grinding process. The experimental results show that the AE signal identification accuracy of the grade is excellent, at 99%. The vibration signal of the wheel surface condition during the grinding process is significant as well, yielding an identification accuracy of 91%. The extracted signal characteristics in this research not only quantify the state of the grinding wheel, but also facilitate a wheel monitoring system based on the identification technology. The proposed method for grinding wheel processing status monitoring can be used to establish an automated intelligent grinding system.

INDEX TERMS Acoustic emission, feature extraction, grinding wheel grade, machine learning, radial and axial vibration, wheel loading.

I. INTRODUCTION

The growing integration of electronic components has contributed to the development of surface grinding techniques that facilitate quick grinding and highly flat finishes, which have been applied extensively in wafer thinning. The grinding of hard and brittle materials is the focus of much recent attention because they tend to resist heat and corrosion, have high hardness values, and have high melting points. One such material is sapphire, whose wide optical transmission band makes it a common material for optoelectronic components. The machining quality of the surface of a thinned sapphire wafer has a direct effect on the quality of an LED product.

Grinding involves using the normal and tangential forces generated through the relative motion between a workpiece

The associate editor coordinating the review of this manuscript and approving it for publication was Li He[ID].

and a disk-shaped grinding wheel to cause the abrasives of the wheel to remove materials, thus achieving high dimensional precision and good surface roughness [1]. A grinding wheel that uses diamond abrasive and has an appropriate grade, with a micro feed rate and a negative rake angle, performs ductile-regime grinding on a hard and brittle material without damaging the surface [2]. Dobrescu and Anghel discuss the relationship between the angular deviation of grinding between a wheel and wafer and the surface profile of the workpiece; the angular deviation of grinding represents the specific energy of grinding [3]. Machining hard and brittle materials requires high specific grinding energy [4].

Hard and brittle materials are generally ground on a grinding wheel with diamond abrasive and a metal binder. The size of the abrasive grain determines the quality of the machined surface and the material removal rate. The binder holds the abrasive against the centrifugal and grinding forces generated

by machining and aids self-sharpening [5], in which worn abrasive comes off the grinding wheel, allowing new, sharp grains to emerge. How well the binder holds the abrasive is referred to as the "grade"; this indicates how easy it is for the grinding wheel to shed the abrasive. A soft grinding wheel is often used to machine workpieces with low material removal rates and high hardness, such as sapphire and silicon carbide wafers. A hard grinding wheel is used on those with high material removal rates and low hardness, such as metals.

Hard and brittle materials are comparable to the abrasives of the grinding wheel in terms of hardness; over the course of the grinding process, grains become dull from wear. When this happens, the chips produced from cutting fill the pores of the wheel surface, flattening the surface and rendering the wheel incapable of cutting [6]. If a flattened grinding wheel continues to operate, however, the normal force (F_N) overtakes the tangential force (Ft), resulting in damage to the workpiece and ruptures in the wheel. Therefore, whether a grinding wheel can machine a hard and brittle material continuously depends on whether the wheel can sharpen itself in a timely manner. Diamond grinding wheels are expensive, and usually have poor self-sharpening capabilities, resulting in rapid consumption; despite the industrial emphasis on such capabilities, this translates to a high wear ratio and high machining costs, making such soft wheels undesirable for typical commercial uses.

Abrasives wear during grinding because of the rubbing between the wheel and the workpiece and because of the compression of the abrasives under high temperature and pressure. In addition, the cutting chips from the workpiece surface fill the pores of the wheel surface, leading to wheel loading. After the abrasives are worn and the pores filled, the wheel surface becomes dull. The contact area with the workpiece increases, the rubbing increases between the surfaces, the wheel's grinding weakens, and it gradually loses its ability to remove chips.

As the wheel loses the ability to grind, its rubbing with the workpiece intensifies, driving up the S1 current load [7]. When the rubbing exceeds the wheel grade, the wheel continues to self-sharpen to maintain its grinding capability, in which case the S1 current load remains constant. Usually, an operator can determine the grinding condition on the basis of the S1 current load, which however provides no comprehensive understanding of the respective condition of the grinder, wheel, and workpiece because the load is a result of the interactions between the three. In this study, other signals are leveraged to enable a more accurate real-time identification of wheel states.

In this study, an intelligent monitoring grinding system is developed for application to the processing test development stage of a new grinding process (a workpiece of new material or a new grinding wheel), which provides intelligent judgment of the grinding status and helps optimize the process.

This paper first reviews the literature on grinding monitoring technology and explains the issues to be solved in this study. Then, two kinds of experiments are conducted to observe the characteristics (wheel grade and surface conditions) of the grinding wheel, and signal analysis is utilized to extract the characteristic signals of grinding processing. Finally, the identification effects of the characteristic signal and the three classifiers with respect to the status of the grinding wheel are compared.

II. MONITORING GRINDING PROCESSES

Grinding is a highly complex process that takes into account the wheel's composition, the workpiece materials, the machining method, the feed direction, the quantity of grinding coolant, and the machining parameters. Together, these factors determine the machining outcome. However, it is difficult to identify whether mishaps are occurring during machining because a number of conditions (such as grinding noise, wheel vibration during operation, and the spraying of coolant) arise during the process, and machining takes considerable time [8]. Any change during machining must be deduced from the machined workpiece. Accordingly, many have focused on techniques that monitor the grinding process in real time.

Acoustic emission (AE) is a high-frequency stress wave that occurs when a material undergoes plastic deformation, specifically due to the material's dislocation slip, phase transition, rubbing, and micro fracture formation. The wave is free from almost all disturbances from machines and the environment because its frequency spans from 10 to 2,000 kHz [9]. Because of these properties, AE is widely used in systems that monitor grinding. Hundt *et al.* demonstrate the feasibility of using AE signals to monitor the grinding wheel's state while it is working [10]. Webster and Dong investigate performance differences in the raw AE signal in time and frequency domains in internal, external, centerless, and surface grinding processes; in their experiments, they employ a hydrophone-type AE sensor, which integrates an AE sensor with cooling water, splashing the cooling water onto grinding areas and sending the AE signals back to the sensor. Thus, its application is not limited by the direction in which the grinding wheel moves [11]. Susič and Grabec use AE signals to evaluate the surface conditions (newly-dressed, slightly-worn, and worn-out) of aluminum oxide grinding wheels used to grind hardened steel materials. They conclude that the characteristics of the AE signal frequency spectrum are more effective than the time-domain root mean square value in determining the wheel condition, although the evaluation results are inaccurate at the beginning of grinding, when the AE signal exhibits little difference [12]. Aguiar *et al.* employ band-pass filters to eliminate the noise of the cutting fluid in the raw AE signal and establish a dressing monitoring system [13]. Liao *et al.* adopt a diamond wheel to perform creep feed grinding on alumina oxide specimens, analyze AE signals through wavelet transforms to explore each signal segment's wavelet-based energy features formed by dull and sharp grains, and apply an adaptive genetic clustering algorithm to distinguish wheel conditions. Their method achieves 97% accuracy under high material

removal rate conditions, 86.7% under low material removal rate conditions, and 76.7% under combined grinding conditions; they mention that the extracted features apply only to certain grinding conditions [14]. Lee *et al.* use AE signals to depict a wheel surface; this visualization approach can aid in dressing and in other evaluation procedures for grinding wheels [15]. Aguiar *et al.* acquire AE signals while an aluminum oxide grinding wheel grinds medium carbon steel. They use different statistical approaches to extract the features and to determine which statistic is most effective in detecting grinding burn; the authors prove that constant false alarm (CFAR), the ratio of power (ROP), kurtosis, and correlation of the AE are all more sensitive than the root mean square (RMS) [16].

In addition to monitoring the grinding condition through AE signals, researchers have used other sensor signals to monitor the grinding process [17]. Hwang *et al.* employ an AE sensor, a power meter, and a force dynamometer to monitor the grinding process, suggesting that the wear of the wheel intensifies as the AE signal amplitude, grinding force, and energy increase. They conclude that the ratio of the AE signal energy to the grinding force can be used to evaluate how worn the wheel is and when it should be replaced [18]. Liu and Li analyze the relationships between load and the AE value across different grinding feed amounts to ascertain whether the AE signal can act as an early warning for grinding load and thus help to improve grinding quality. The authors argue that the AE signal is merely one of the factors that predicts grinding load. They argue that more data and factors should be taken into account to facilitate a more accurate prediction of grinding load when the AE signal is used to monitor instantaneous changes in grinding load [19]. Chang *et al.* diagnose and predict the machining state on the basis of the main spindle vibration signals of the horizontal grinder, and extract the time-domain and frequency-domain features of the vibration signals as well as the quality of the machined parts, incorporating them into a statistical machining control graph to visually monitor changes in the parameters during machining; they determine the machining quality accordingly [20]. Badger *et al.* use AE intensity and a dynamometer to establish the relationship between dressing energy and AE, to investigate how different grinding contact modes affect the AE amplitude, and to quantify dressing efficiency, wheel sharpness, and wheel dullness [21].

Regarding grinding conditions, scholars have analyzed AE signals, extracted features, and incorporated them into supervised or unsupervised machine learning algorithms to formalize models for monitoring grinding conditions. Liao *et al.* use minimum distance classifiers to construct an online system for detecting dull grinding wheels [22]. Marec *et al.* extract AE features through wavelet transforms and perform fuzzy C-means clustering (an unsupervised classification method) to cluster the damage characteristics of glass fiber reinforced polymers [23]. Others have used neural networks to identify grinding conditions. Wang *et al.* use a neural network to identify grinding burn after comparing different algorithms

for extracting AE features [17]. In [24] and [25], neural network algorithms are used to identify AE features, determining different grinding conditions: normal, burning, and chatter vibration. Martins *et al.* extract the AE signal from a worn grinding wheel, compare the accuracy between the RMS and ROP through neural network models, and conclude that the ROP is more accurate than the RMS [26]. Lin *et al.* furnish a metal grinder with multiple sensors; they extract eight features using an AE sensor, a vibration meter, and a force measuring unit. Then they apply a neural network and fuzzy-logic-based system to identify wheel conditions [27].

These studies do not touch upon the monitoring of the grinding wheel's grade. Studies related to grinding wheel monitoring predominantly focus on the grinding of metal materials and fail to incorporate wheel grade as a factor affecting machining conditions. Diamond wheels are different from traditional wheels because there is no wheel grade classification such as from A (soft) to Z (hard) for diamond wheels. However, wheel grade is a critical factor in the grinding of hard and brittle materials because it affects the self-sharpening capacity of the wheel. On a typical grinder, only the change in the electric current load of the grinding spindle can be observed; the wheel's grade cannot be determined or quantified through the current of the main spindle during grinding. However, as sapphire wafers are designed with increasingly large diameters, they become increasingly difficult to machine; numerous manufacturers of grinding wheels and grinders strive to improve the wheel's quality and machining efficiency through online monitoring and quantification of the wheel's grade [28].

Table 1 compares wafer defects across different grinding wheel states. Unlike ground metal materials, the defects of machined hard and brittle materials are identifiable only via offline measurements. Experienced engineers directly observe defects on machined wafers to infer the causes of defects; doing so entails considerable labor and cost.

TABLE 1. Grinding defects and wheel states.

State of grinding wheel (cause of defect)	Wafer defect			
	Surface burn	Flutter textures	Surface scratches	Bad total thickness variance
Grade too hard	●	●		●
Grade too soft		●	●	
Stuffing of pores	●			
Wearing of grain	●			
Exception vibration		●		●

Table excerpted from a grinder operation manual [28].

In this work, an AE sensor, a two-axis (radial/axial) accelerometers, and a three-phase current transducer are used

to capture signals of various wheel states throughout the grinding process and to extract features to determine the wheel's grade and state. These results constitute a reference for operators to predict potential wafer defects in current or subsequent stages of the grinding process given their assessment of the wheel state and thus address issues before defects occur.

III. TEST BENCH SETUP AND DIAMOND GRINDING WHEELS

The grinder used in this study is a vertical grinder that performs vertical grinding by rotation of its upper and lower spindles, as shown in Figure 1 (a). This setup, which allows for favorable flatness and thickness precision, is applied extensively in the thinning of silicon or compound wafers, which are to be made highly flat. The upper spindle is a grinding spindle with the grinding wheel installed; it rotates at a high rate during operation. In the present study this is referred to as "S1". The lower spindle holds the workpiece. Using wax, a wafer is attached onto a ceramic disk before being machined and the disk is then secured through vacuum to the platform for the lower spindle, which rotates slowly. In this study the lower spindle is referred to as "S2". During grinding, S1 descends slowly to thin the wafer on S2. The grinder contains a feed system with high precision, stability, and stiffness that conducts micrometer feeding; its

(a)

(b)

FIGURE 1. (a) Precision vertical grinder and monitoring system for grinding process. (b) Configuration of headstock and accelerometers.

direction of motion is along the Z-axis. The angular deviation of the grinding wheel to the workpiece is referred to as the angular deviation of grinding, which improves the grinding force as it increases. However, excessive grinding force may result in damage to the wafer and the grinding wheel.

In these experiments, a 12-inch diamond abrasive grinding wheel with 36 tooth-shaped abrasives was adopted; these specifications are often used to grind sapphire wafers in industrial contexts.

As the vertical grinder operates, S1 and S2 rotate simultaneously (S1 rotates clockwise and S2 counter-clockwise, viewed from the top), making it impossible to attach a wired AE sensor to the grinding wheel or workpiece. Thus, a hydrophone AE fluid sensor made by Balance Systems was used in the experiments. This sensor stabilizes cooling water to enable noncontact transmission of signals and operates at frequencies from 10 k to 1 MHz. The raw AE signal was sampled at a frequency of 5 M/s using a PCI-6111 data acquisition card. Clean cooling water was discharged onto the aluminum ring of the grinding wheel to transmit signals, because stress waves propagate through a medium. Industrial vibration sensors supplied by Wilcoxon Research were used for accelerometers 1 and 2; the model number was 786A, with a sensitivity of 100mV/g NOM. The sensors were installed on the headstock of the S1 bearing using magnets, as shown in Figure 1 (b). Accelerometer 1 measured the radial vibration signals, and accelerometer 2 evaluated the axial vibration signals. Signals were sampled through the NI-9234 card (made by National Instruments) at a frequency of 10,240 s/ch. The current transducer was made by LEM (model: HTR 100-SB) and was mounted on the U, V, and W lines of the frequency converter for the S1 motor to measure changes in the motor load during grinding. The signal extraction module, which shared a chassis (CompactDAQ) with the accelerometer module, captured signals through the NI-9234 card (National Instrument) at a frequency of 10,240 s/ch. When the signal extraction system was on, it synchronized the signal data of the AE, vibration, and current sensors.

Five grinding wheels with #400 diamond abrasives and various grades were used in grinding experiments, as described in Table 2. The wheel surface images were obtained using a digital microscope (500X). The diamond wheels were grinding wheels with artificial diamonds bonded to the periphery; as these are non-traditional abrasives, the wheel grades are not clearly defined. In the industry, this is typically determined using the ratio of wear (ROW), which represents the ratio of the removal of the workpiece to that of the wheel after grinding. The five wheels are ordered from left to right according to the ROW: from the hardest wheel (row0001), which barely self-sharpens, to the softest (row3). The ROW value of each wheel is defined by its manufacturer through tests; in the industry, row005 wheels are often used to grind sapphire wafers.
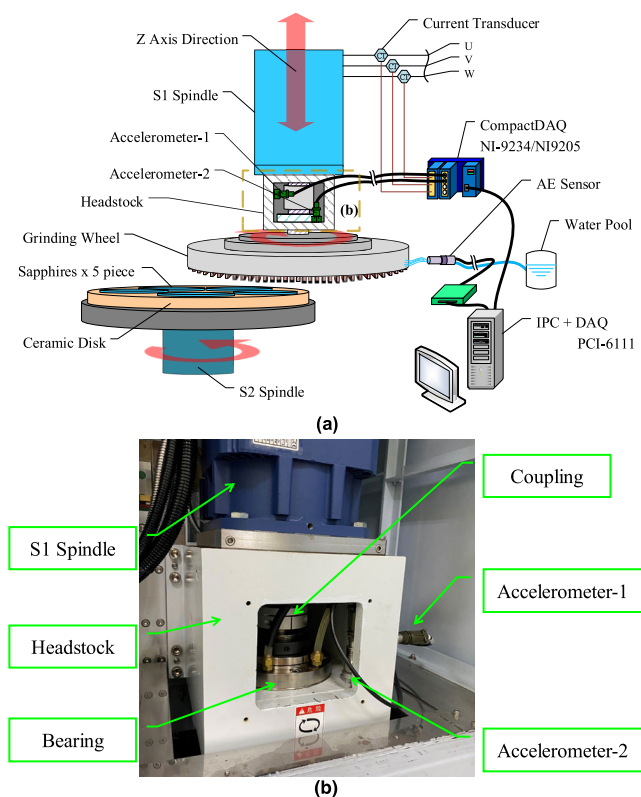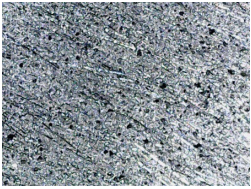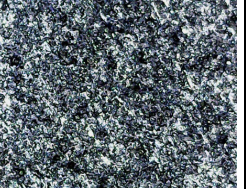
TABLE 2. Diamond grinding wheel specifications.

row0001	row005	row01	row1	row3
Abrasive: diamond	Abrasive: diamond	Abrasive: diamond	Abrasive: diamond	Abrasive: diamond
Binder: metal	Binder: metal	Binder: metal	Binder: metal	Binder: metal
Grain size: #325	Grain size: #400	Grain size: #325	Grain size: #325	Grain size: #325
Ratio of wear (ROW): 1:0.001	Ratio of wear (ROW): 1:0.05	Ratio of wear (ROW): 1:0.1	Ratio of wear (ROW): 1:1	Ratio of wear (ROW): 1:3

The grain size (#) is determined by the number of sieve holes that cover a straight, 1-inch long line. The larger the number, the finer the abrasive.

The ratio of wear (ROW) is the ratio of the thickness of the workpiece to the grinding wheel after grinding. For instance, 1:0.05 indicates that the thickness of the sapphire was reduced by 1 mm, and the thickness of the grinding wheel was reduced by 0.05 mm.

Images of wheel surface obtained using a digital microscope (500X).

IV. EXPERIMENTAL METHOD

A. GRINDING WITH DIFFERENT GRADES OF GRINDING WHEEL

Table 3 lists the experimental grinding recipe for the vertical grinder. This recipe consists of speed parameters for S1 and S2 and feed rate parameter Z for sapphire wafer processing using row005 grinding wheels. The S1 speed generally ranges from 600 to 1,400 rpm, whereas that for S2 ranges from 50 to 120 rpm. Speeds in excess of these ranges tend to result in abrasive teeth fractures in the grinding wheel. The grinding feed rate is based on the characteristics of the grinding wheel, for example, wheel grade, grain size, etc. Excessive feed rates cause the wheel to fracture and the wafer to break, and rates that are too slow reduce grinding efficiency.

TABLE 3. Grinder recipe.

Parameter	Specification
Peripheral speed of grinding wheel (S1)	1,000 rpm
Peripheral speed of workpiece plate (S2)	60 rpm
Grinding feed rate (Z-axis)	0.06 mm/min
Grinding thickness	0.2 mm
Cooling flow rate	15 L/min

The five grinding wheels were used to perform grinding three times at a feed quantity of 0.2 mm along the Z-axis; the grinding process was completed when the grinder shut down after it reached the feed height or the main spindle became overloaded. Before each experiment trial, the wheel surface was dressed for 0.05 mm to ensure a consistent contact-area angle between the grinding surface of the wheel and the workpiece disk and a consistent wheel state. Five 4-inch sapphire wafers were used as workpieces and glued on to a 12-inch ceramic disk with wax in a circular pattern at 10-mm intervals. The flatness of each wafer was under 10 μm after being glued.

B. CHANGE THE SURFACE CONDITION OF GRINDING WHEEL DURING GRINDING

In the experiments, as it had the most suitable hardness, the row005 wheel was observed, in particular, the change of the grinding wheel surface during the grinding process. The grinder recipe mirrored the previous experiment shown in Table 3. In this experiment six grinding cycles were performed using only the row005 wheel and a 0.2 mm grinding thickness. Before each grinding cycle, the grinding wheel was dressed for 0.05 mm to ensure a consistent wheel surface state. To aid in the transition of abrasives from sharp to dull and in the transition of pores from empty to filled, five 4-inch sapphire wafers were glued onto a 12-inch ceramic disk, adjoining one another (generally, the experimental setup was the same as that of the earlier experiment: the five 4-inch sapphire wafers were glued onto a 12-inch ceramic disk at 10-mm intervals). This procedure increased the wheel's area of contact with the workpiece within each unit of time, undermining the wheel's ability to remove chips, allowing rubbing to increase, and prompting the wheel to apply greater cutting force. In addition, this procedure accelerated the dulling of the abrasives and the filling of surface pores.

V. EXPERIMENTAL RESULTS AND DISCUSSION

A. THE PERFORMANCE OF DIFFERENT GRADES OF GRINDING WHEEL

Throughout each grinding experiment, the raw AE signal, the axial vibration signal, the radial vibration signal, and the S1 current were recorded, as was the state signal of the wheel undergoing a dry run. During the experiment, in which each wheel performed grinding three times, the row0001 wheel failed to complete any of the three trials of grinding at a feed quantity of 0.2 mm because a current overload protection mechanism for the S1 motor was activated by default when the grinder was operating. What caused the current load of S1 to continue increasing was that the

row0001 wheel had such a high grade that the wheel hardly self-sharpened at all while it was grinding, and that rubbing intensified between the wheel and the workpiece after the wheel lost its cutting force while the feeding continued along the Z-axis [29]. This protection mechanism prevented the excessive normal force from fracturing the wheel. The current load for the main spindle in a dry run was 37%; warnings were issued when the load reached 40% during grinding, and the grinding wheel stopped working when the load increased to 41%.

Figure 2 depicts the level of wear sustained by the five grinding wheels in the experiments. Notably, the row0001 wheel, which had the hardest grade and should have the least wear, was experimentally shown to have had more material removed than did the row005 and row01 wheels. Drawing on our experience, we assumed that because the grade of row0001 was approximately 41% spindle loading, the abrasives became detached when the wheel stopped working. Additionally, because the abrasives were held tightly together, they detached in large lumps when the wheel was self-sharpening. The row3 wheel had the most wear because it continued self-sharpening during grinding.
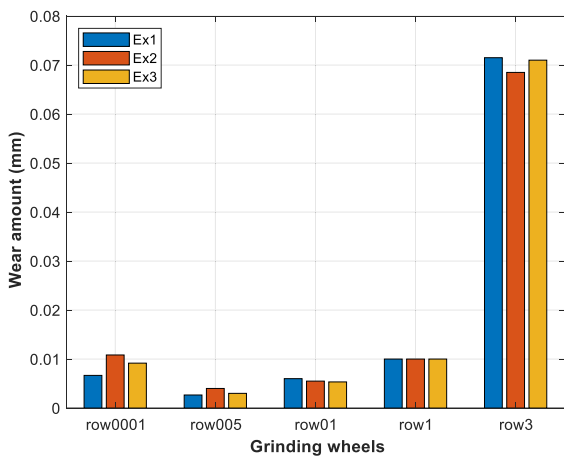

FIGURE 2. Amount of wear in grinding wheel after 3 experiments for each of 5 wheels. For each grinding wheel, 3 teeth were selected to measure the abrasive height; these values were then averaged to produce the graph data.

Figure 3 shows the removal level of the sapphire wafers in the grinding experiments. To successfully grind hard and brittle materials, a grinding wheel must apply an adequate normal force on the material, which results in bending stress because of the non-collinearity of the normal force between the wheel and the workpiece [30]. As this changes the aluminum frame of the wheel in feeding, a 1:1 ratio between the amount of removal and feeding is unattainable, complicating the estimation of the grinding thickness of such materials. Although row0001 did not complete its feeding procedure, its cutting force was so high that it achieved considerable material removal; nevertheless, the wheel and the workpieces were all prone to damage. The lowest grinding efficiency was
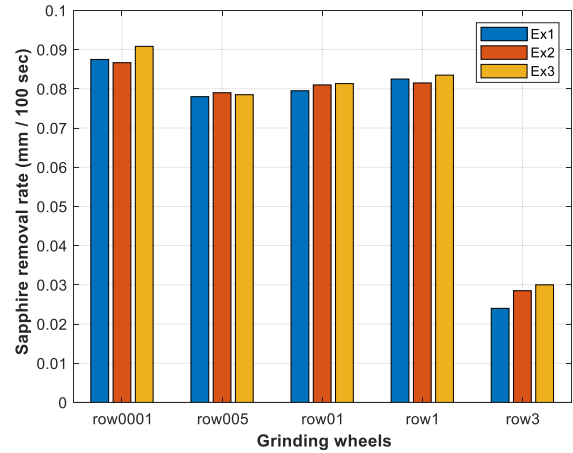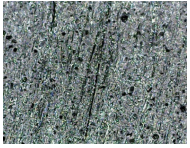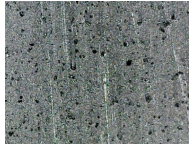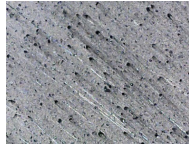

FIGURE 3. Removal rate from sapphire wafer after grinding. Five 4-inch wafers were ground at the same time in each experiment. The removal amount was measured as the 3-point average of a single piece; the average thickness of the 5 pieces was then averaged again.

found in row3, which had such a soft grade that the wheel shed abrasive as soon as it touched the wafer.

B. DISTINGUISHING GRINDING WHEEL SURFACE CONDITIONS

Table 4 presents images of the row005 surface obtained using a digital microscope (500X) after the wheel was dressed, after continuous grinding experiments, and after losing the ability to grind.

TABLE 4. Surface condition of grinding wheel.

row005		
Wheel surface after dressing (sharp)	Wheel surface after grinding (mid)	Wheel surface after spindle overloading (dull)

Images of wheel surface obtained using a digital microscope (500X).

Initially, the surface of the dressed row005 wheel is clean, with conspicuous diamond abrasives and pores. The surface after continuous grinding experiments is relatively smooth, with most of the pores filled by chips. The wheel's diamond abrasives are mostly conspicuous. The surface of the row005 wheel that has lost the ability to grind, whose image was captured after S1 was overloaded during grinding, shows hardly any pores. Moreover, comet-like traces are observed along the grinding direction on the diamond abrasives; this indicates that few diamonds are exposed on the surface and that other abrasives are covered by chips [31].

However, the five sapphire wafers, which were attached with each adjoining one another onto the disk, were more difficult to grind. As a result, when S1 became overloaded

during grinding, the wheel continued self-sharpening at the edge of overload and thus recovered its grinding capability. This allowed the researchers to chart how the wheel's state changed throughout the grinding process.

Figure 4 shows the changes in the AE root mean square and the S1 current in the third grinding cycle. Both signals increased gradually when the wheel was worn and its surface filled. However, they picked up in different slopes, suggesting that they differed in physical quantity. Both signals decreased after approximately 200 sec, when the wheel began self-sharpening to recover its grinding capability. Figure 5 presents the root mean square of the radial/axial vibration and the S1 current in the third grinding cycle. These results suggest that the two vibration signals reveal grinding information that is different from AE.
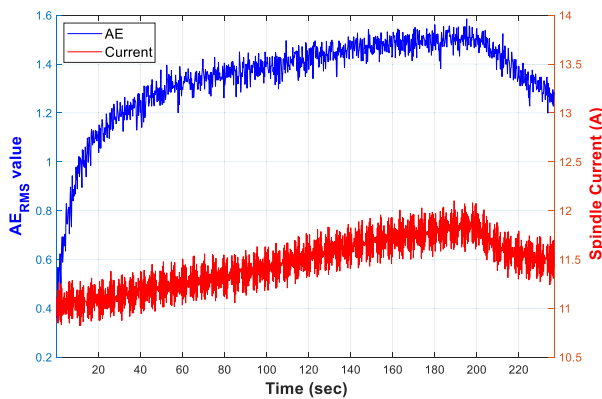

FIGURE 4. Root mean square of AE signal and S1 current from grinding process of adjoining wafers.
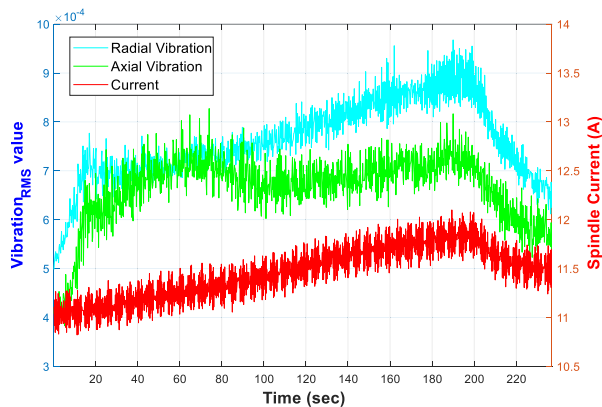

FIGURE 5. Root mean square of radial/axial vibration signal and S1 current from grinding process of adjoining wafers.

VI. CHARACTERISTIC SIGNALS ANALYSIS AND FEATURES SELECTION AND EXTRACTION

Because a hard and brittle workpiece is as hard as the abrasives of the grinding wheel, the wheel sustains considerable wear when it grinds the workpiece. Thus, self-sharpening is seen as a critical factor in enabling continuous grinding using such a wheel. This is why manufacturers of grinding wheels develop multiple abrasive formulas for different workpieces and grinders. Even when a manufacturer puts its own grinding

wheel into service for the first time, they must test the wheel to determine its grade. Thus, this study utilizes characteristic signals to quantify the grinding wheel grades so that operators can assess the wheel states [32].

A time-frequency analysis was performed on the AE signals obtained during grinding. The set of raw AE signals had 5 million data points for each second of grinding. Due to the large amount of data, to retain the details, this was divided into segments of 1 million data points for analysis, which was equivalent to 0.2 s of grinding, during which the wheel completed 3.3 turns.

A. ROOT MEAN SQUARE (RMS) OF TIME DOMAIN ANALYSIS

As the raw AE signal is a time-variable voltage value, the RMS, as expressed by (1), is often used to estimate the mean deviation of the signal. Many studies use the RMS of the AE signal to characterize time-domain features. For the relatively hard grinding wheels, row0001 and row005, AE_{RMS} values increased slowly with grinding time and then stabilized. The three softer wheels had relatively constant AE_{RMS} values regardless of grinding time.

$$x_{RMS} = \sqrt{\frac{1}{N}\sum_{n=1}^{N}|x_n|^2}, \qquad (1)$$

where x_n is the signal voltage and N is the number of root mean square calculations. Here, the vibration RMS is vibration$_{RMS}$ and the spindle current RMS is current$_{RMS}$.

The power spectrum of the AE signals suggests that while the sharp wheel surface became dull and then self-sharpened throughout grinding, the feature band in the spectrum did not shift, but the power value changed. The power increased gradually and then stabilized as the wheel surface became dull and had its chips loaded in grinding.

B. RATIO OF POWER (ROP) OF FREQUENCY DOMAIN ANALYSIS

Figure 6 presents the power spectra of the AE signals for the five grinding wheels, where feature bands are observed in the segments of (ii) 200 to 500 kHz and (i) 550 to 950 kHz. Wheel of different grades have different power spectrum densities [33]. The ROP, as expressed by (2), is a statistical method used to estimate the band power density ratios in the power spectrum. It can be used to determine the ratio of a given frequency band to the full spectrum. In this study, the segment from 100 to 999 kHz was divided into 9 bands at a 100-kHz interval on the basis of the AE sensor's frequency range.

$$x_{ROP} = \frac{\sum_{k=n_1}^{n_2}|x_k|^2}{\sum_{k=0}^{N-1}|x_k|^2}, \qquad (2)$$

where the denominator is the entire power spectrum, N is the number of frequency data points in the spectrum, the
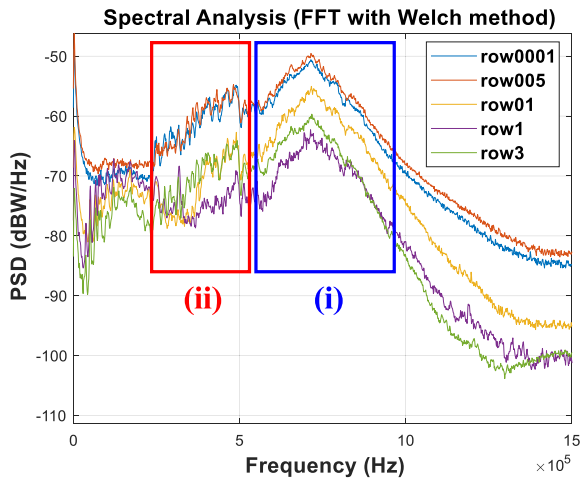
FIGURE 6. Power spectrum density of AE signal at 100th second in grinding process of each of 5 grinding wheels. Note that the characteristic frequency band of the frequency spectrum does not move significantly during the grinding process.

numerator is the spectral power for the observed band, and n_1 and n_2 are the limits of the band.

C. SLOPE OF POWER SPECTRUM (SOPS)

As the grinding time increased, the wheel surface became smoother, and the power spectrum density (PSD) of the band segment (i) increased gradually to a stable level. This change was most prominent for row0001 and row005. The PSD difference on a given band was quantified by estimating the SOPS. The SOPS estimation covered the band from 600 to 700 kHz.

D. CHARACTERISTICS OF DISCRETE WAVELET TRANSFORM (DWT)

Several feature bands were identified on the power spectrum of the AE signals. The characteristic signals were extracted from the frequency bands via a discrete wavelet transform per functions (3) and (4) and then statistically analyzed [34]:

$$x_{p,L}[n] = \sum_{k=0}^{K} x_{p-1,L}[2n-k]LPF[k], \qquad (3)$$

$$x_{p,H}[n] = \sum_{k=0}^{K} x_{p-1,H}[2n-k]HPF[k], \qquad (4)$$

where the input signal $x[n]$ length is N, while the coefficient length of $x_{p,L}[n]$ and $x_{p,H}[n]$ at the p-th level is $N/2^p$. In this work, the mother wavelet is Daubechies 10 (Db10).

The wavelet packets are represented by the stage structure (p, q). where p is the number of levels of wavelet packets, q is the coefficient of the levels of the wavelet packets, and q is 2^p. Figure 7 shows the 4-level filter bank used in this study. The packet (3, 1) coefficients were high-frequency data that contained most of the energy of spectral power. The packet (4, 1) coefficients were low-frequency data that contained limited energy of spectral power but exhibited feature

changes that differed from the packet (3, 1) coefficients in the power spectrum throughout the grinding process.

Statistical methods were employed to calculate two groups of coefficient features [35]: **standard deviation (STD)**, **L2 norm**, **entropy**, **mean absolute**, and **median absolute deviation**. In particular, entropy is a measure of randomness that represents the disorderliness of the data. **Entropy** calculation was utilized as in image data entropy algorithms, converting data to 8-bit unsigned integers for histogram-based counting. The data were then normalized and substituted into the equation for information entropy, as expressed by (5):

$$H(x) = -\sum_{i=1}^{n} p(x_i) \log_2 p(x_i), \qquad (5)$$

where p is the probability mass function of random variable x and $H(x)$ is information entropy, whose unit "bit" denotes the amount of data.

The aforementioned statistical methods were used to reveal the trends of feature data throughout grinding. The entropy trends are mostly similar between the (3, 1) and (4, 1) coefficients, but the entropy feature trends for row0001 and row005 indicate how the wheel surface state changed. Indeed, as the grinding time increased, the entropy of the two grinding wheels in light of the (3, 1) coefficients decreases and becomes increasingly stable (Figure 8). This suggests that the disorderliness of the coefficients declined slowly, reflecting how the wheel surface became smooth as its pores were filled and the surface was worn. By contrast, the entropy of the (4, 1) coefficients surges and then reaches a stable state. However, the entropy of the (3, 1) and (4, 1) coefficients for the soft grinding wheels—row01, row1, and row3—exhibits no significant changes because they were constantly self-sharpening during grinding. In Figure 8, the entropy for row0001 stops at 174 s because S1 became overloaded during grinding, interrupting the grinding process. Given these results, the entropy of the (3, 1) coefficients had a strong connection with the wheel state.

E. DATA SCALING

This is a form of data preprocessing. This study uses a minimum and maximum scaler (min-max scaler) to move all data to the range between 0 and 1 in order to observe the data distribution.

The raw AE signal was converted into 21 features: rms, rop1, rop2, rop3, rop4, rop5, rop6, rop7, rop8, rop9, dwt31_std, dwt31_norm, dwt31_entropy, dwt31_mean, dwt 31_med, dwt41_std, dwt41_norm, dwt41_entropy, dwt41_mean, dwt41_med, and SOPS. Figure 9 is a boxplot depicting the 21 features for the five grinding wheels undergoing the dry run and the three experimental trials. To determine how the wheel differed in terms of each feature, all the features were scaled via a min-max scaler to the range between 0 and 1. It was found that the RMS differed substantially between the dry run and grinding process. The ROP variance was noticeably different across different grades
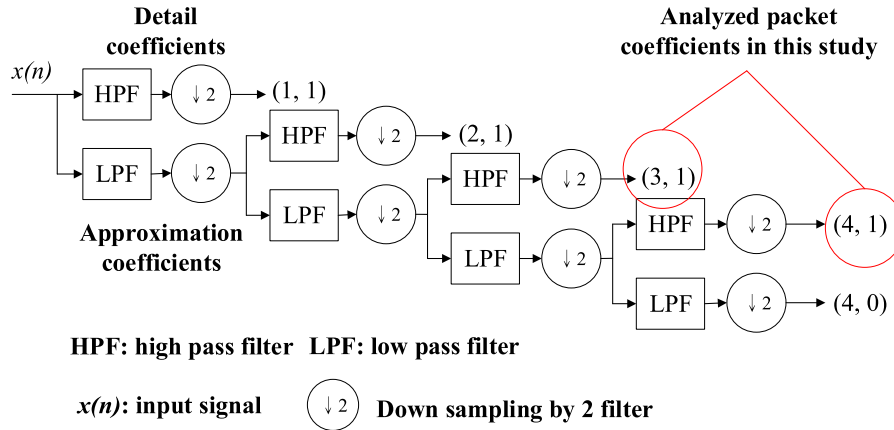
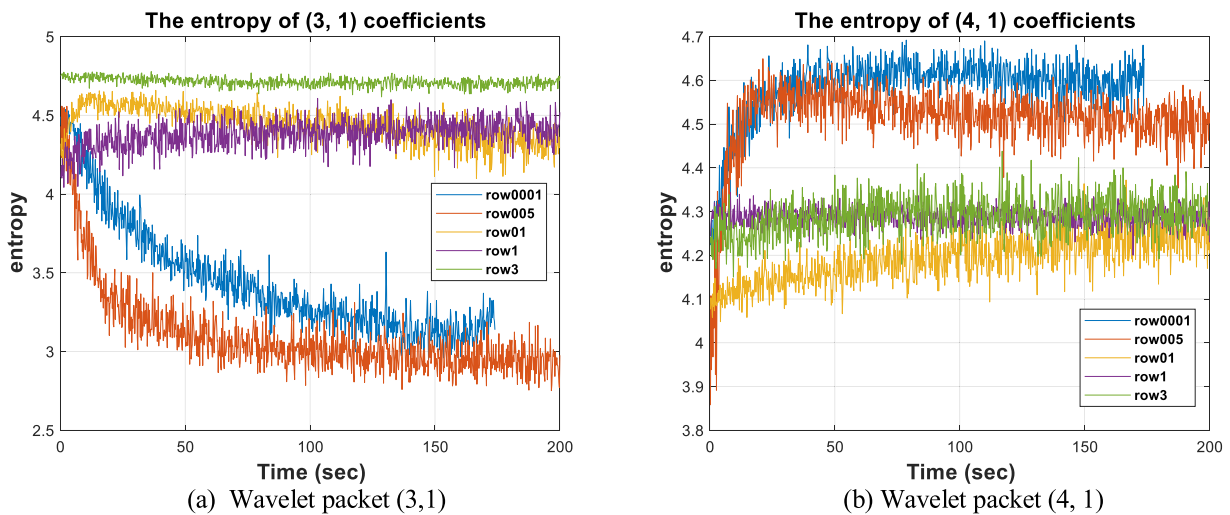**FIGURE 7.** Four-level signal decomposition into packet coefficients.

FIGURE 8. Entropy of wavelet packet (3, 1) and (4, 1) coefficients from five grinding wheels in second grinding experiment.

of the grinding wheels; the most prominent differences in variance were observed among rop6, rop7, and rop8 for row01 and row1, which were soft wheels that were alternately compressing and self-sharpening throughout grinding. However, the three band segments for rop6, rop6, and rop8 best represent the wheel state. Of the five dwt31 features, the distribution of features for the hard row0001 and row005 wheels appears opposite to that of features for the soft row01, row1, and row3 wheels; those parameters exhibit no prominent features during the dry run. The variances of the five dwt41 features are higher for the hard row0001 and row005 wheels than for the soft wheels. The median and variance of SOPS are the highest for row005, a grinding wheel of a type commonly used in industrial applications.

Radial and axial vibration signals were analyzed to identify wheel states. Time-series features were extracted from the raw vibration signals. In this study we used the following time-domain statistics: **RMS** (1), **mean value**, **standard deviation**, **variance**, and the **one-step autocorrelation** function [36]. The one-step autocorrelation function, as expressed by (6), denotes the correlation between a data point and the

subsequent data point and thus better reflects the periodic change of a signal. The signals were calculated based on the time series to reveal feature changes along the grinding process.

$$\rho_\tau = \frac{1}{N-1} \sum_{i=1}^{N-1} x_i x_{i-\tau}, \qquad (6)$$

Frequency-domain features for the vibration signals were calculated based on a time-frequency spectrogram acquired via a short-time Fourier transform (STFT). A time-frequency spectrogram depicts the change of a signal in a given time point within a 3-dimensional matrix of time × frequency × amplitude [37].

Figure 10 shows the changes in the three characteristic signals during the experiment to distinguish the grinding wheel surface conditions. From the spindle current loading on the bottom, the spindle current load is seen to gradually increase due to the dulling of the grinding wheel; AE_{RMS} similarly increases. The red dotted line is the spindle current (A) converted to the drive loading ratio (%).
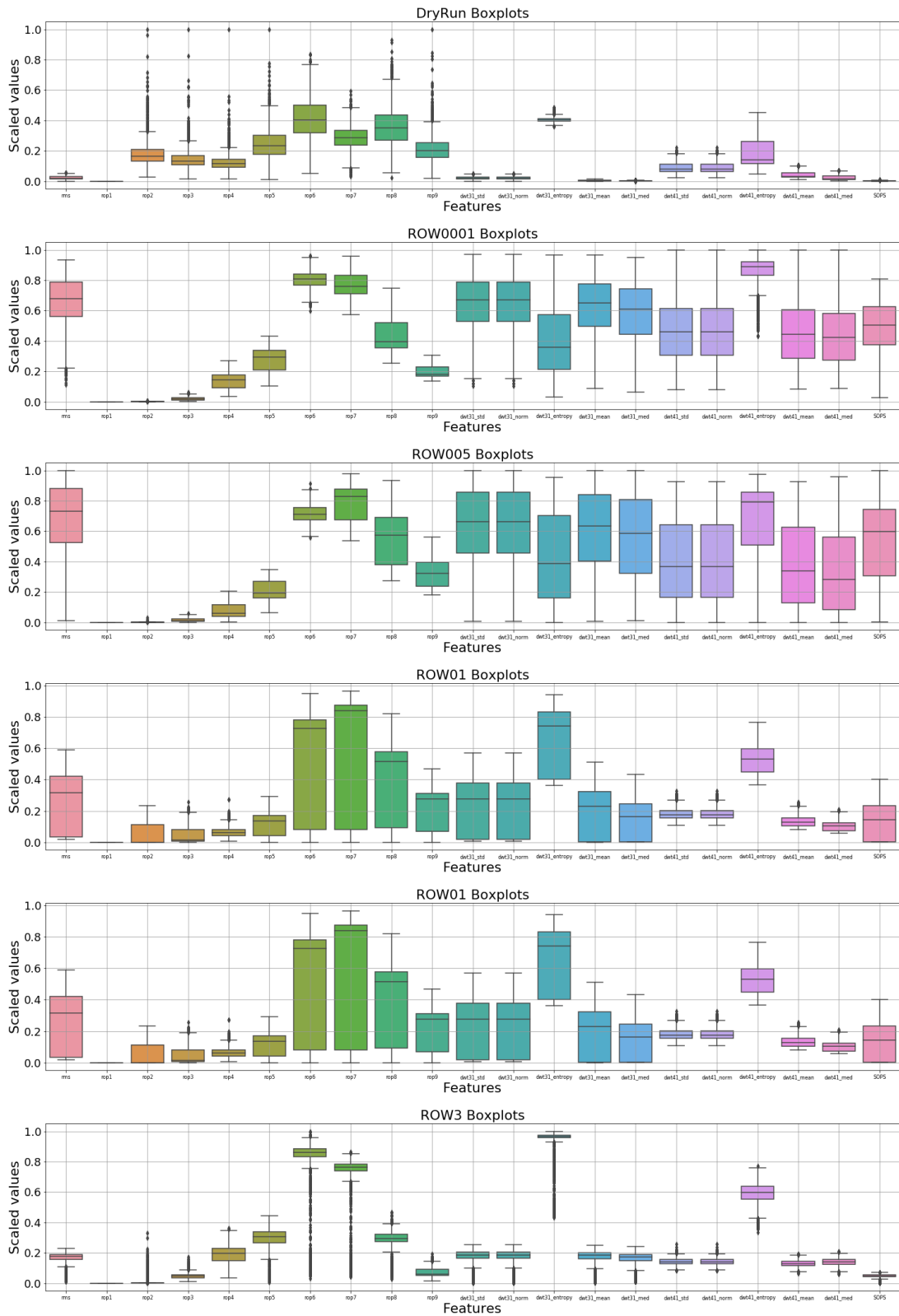
FIGURE 9. Distributions of 21 features of various grinding wheels (dry run + five grades) during grinding experiment. The boxplot features have been scaled.
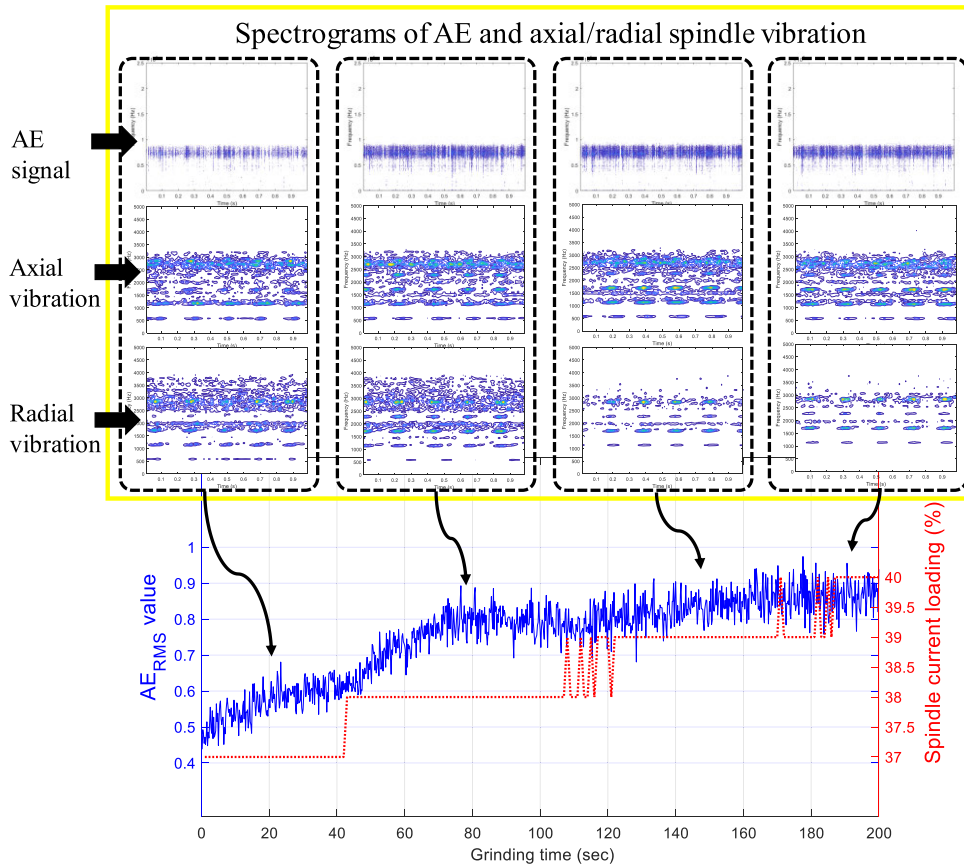
FIGURE 10. Time sequences of AE$_{RMS}$ and S1 current loading (below) and spectrogram of AE, axial, and radial vibration at selected points during grinding experiment (above).

The loading ratio is 37% during the spindle dry run, and the grinder warns and then ceases operation when the loading ratio reaches 41%; the blue line is AE$_{RMS}$. The spectrograms on top for the various time points are the AE signal and axial and radial vibration signals: the vibration signals vary greatly in the sharp and dull conditions.

In this study, the spectrogram was used to determine the **full-time mean value of segmented spectra**, in which all elements in the selected band were summed and averaged along the time axis to obtain the full-time mean for the particular frequency band (7) [38]. In (7), $\mu_{ss}(k)$ is the full-time mean value of the k-th band, N is the number of band matrix elements, f_{lk} and f_{uk} are respectively the upper and lower limits for the k-th band, S is the matrix following the STFT, m is a frequency vector, and n is a vector of a time instant. Given the full-time mean value, n means full columns.

$$\mu_{ss}(k) = \frac{1}{N} \sum_{m=f_{lk}}^{f_{uk}} |S(m, n)|, \qquad (7)$$

The sampling frequency of the vibration signals was 10, 240. The length of the STFT window function was 256, and the window overlap was 50%. Processing the segmented signals through the STFT yielded 129 frequency-band vectors, which were then divided into 13 segments; therefore, k ranges from 1 to 13.

Given the aforementioned time-series and spectrogram features, 18 features were extracted from the raw vibration signals. Thus, each vibration signal had 18 radial and axial features [39].

VII. MACHINE LEARNING-BASED IDENTIFICATION OF GRINDING WHEEL

A. IDENTIFICATION OF GRINDING WHEELS WITH DIFFERENT GRADES

Machine learning algorithms were used to identify six classes: the dry run, and the five grinding wheels with different grades. Table 5 presents the six classes and their respective data matrix shapes.

The six grinding classes were identified through three popular supervised machine learning algorithms: k-nearest neighbors (k-NN), artificial neural network (ANN), and support vector machine (SVM). A k-NN is a simple algorithm that entails little calculation, time, and storage cost; it is often used to perform quick classifications [40]. The ANN is arguably the most popular type of machine learning algorithm because of its breakthroughs in deep learning and computer science. Nevertheless, because in this study we sought to implement a real-time monitoring system, and the raw AE signals had already been characterized, a relatively simple multilayer perceptron with a low calculation
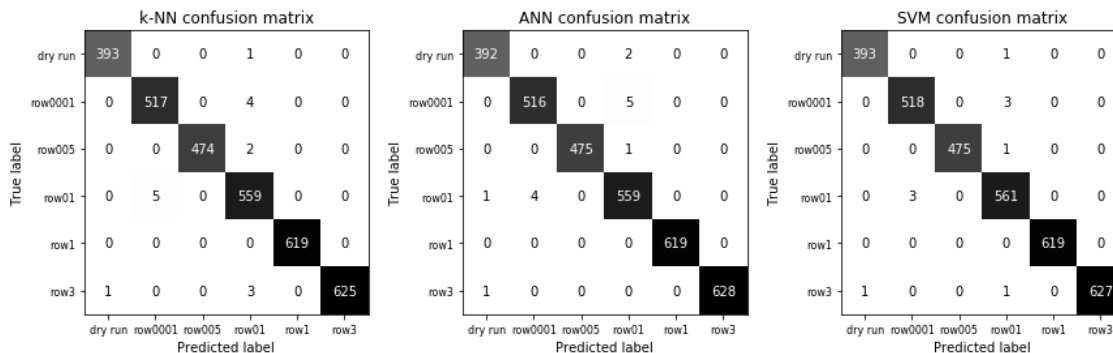
FIGURE 11. Confusion matrix of 3 models for 6 classes.

TABLE 5. Data shape from 6 classes.

Class	Data shape
Dry run	(2130, 57)
row0001	(2605, 57)
row005	(2500, 57)
row01	(2760, 57)
row1	(3005, 57)
row3	(3015, 57)
Total data	(16015, 57)

TABLE 6. Classifier model parameters.

Classifier	Parameter
k-NN	$K = 4$
ANN	activation function = relu
	hidden layer = [20, 20]
	max iterations = 500
	alpha = 0.02
	learning rate = constant
SVM	kernel = rbf
	$C = 10$
	gamma = 10

load and a simple model was used as an ANN [41], [42]. After testing, the ANN showed higher prediction accuracy under five layers. An SVM is a decision machine that minimizes the statistical risk to estimate the hyperplane of a class, to locate a decision boundary, and to maximize the margin (the smallest distance between the decision boundary and any sample) between two classes. An SVM uses only a part of the support vectors to make hyperplane decisions, without relying on massive data; it yields high classification accuracy and delivers high generalization performance [43].

Data were scaled via the min-max scaler, and principal component analysis (PCA) was used to compress the 21 features into 6. All the features were shuffled after they had been connected with their respective classes, with 80% of the total data used for training and the remaining 20% used for testing.

Table 6 shows the respective parameters for the three classifiers. The classifiers were trained and tested, and a pipeline program was used by which a model and multiple sets of parameters were cross-trained and tested, and the prediction results of each parameter were compared to find the best model [44]. A pipeline program is a programming technique that simplifies repeated instructions and series of model training procedures. It realizes streaming workflows and the management of model training steps. Table 7 shows the prediction accuracy of each classifier using the F1 score (8), a way to calculate accuracy using the confusion matrix. The F1 score accounts for both precision (9) and recall (10) to reflect accuracy of this model in a balanced way [45]. Figure 11 shows

the confusion matrix of the testing data for each classifier.

$$F1\ score = 2 \times (precision \times recall)/(precision + recall), \tag{8}$$

$$precision = TP/(TP + FP), \tag{9}$$

$$recall = TP/(TP + FN), \tag{10}$$

where TP = true positive, FN = false negative, FP = false positive, and TN = true negative.

The prediction results suggest that the selected features were highly discriminative. The prediction accuracy exceeded 99% among the three classifiers; SVM was the most accurate. Several pieces of data that belonged to row0001 were incorrectly assigned to row01, as indicated by the confusion matrix.

Given that the abrasives of the grinding wheels tend to fracture during grinding due to human error, two sets of experimental signals with respect to the fractured teeth of the row005 wheel (2,060 data points in total) were obtained under the same experimental conditions to determine whether these signals had any effect on the classification of wheel grades. Table 8 presents the data shapes for the six grinding-wheel classes with said signals taken into account; the training and testing data constituted 80% and 20% of the total data, respectively. Training and prediction were performed with the same classifiers and parameters.

Table 9 presents the prediction results with the signal data of grinding wheels holding fractured teeth. The prediction results were arranged into a confusion matrix (Figure 12).
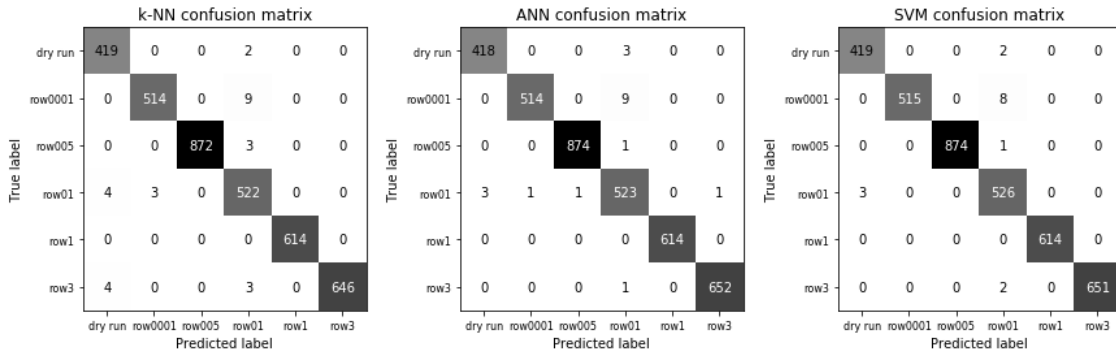
FIGURE 12. Confusion matrix of 3 models for 6 classes.

TABLE 7. Prediction results for grinding wheel grade.

Detection sensor	Prediction accuracy (%)		
	k-NN	ANN	SVM
Acoustic emission	99.3	99.3	99.7

Prediction accuracies measured in terms of F1 score.

TABLE 8. Data shape from 6 classes.

Class	Data shape
dry run	(2130, 57)
row0001	(2605, 57)
row005 (fractured teeth added)	(4560, 57)
row01	(2760, 57)
row1	(3005, 57)
row3	(3015, 57)
Total data	(18075, 57)

TABLE 9. Prediction results for grade of grinding wheel.

Detection sensor	Prediction accuracy (%)		
	k-NN	ANN	SVM
Acoustic emission	99.4	99.5	99.7

Prediction accuracies measured in terms of F1 score.

TABLE 10. Classifier model parameters.

Classifier	Parameter
k-NN	$K = 3$
ANN	activation function = relu
	hidden layer = [50, 50]
	max iterations = 500
	alpha = 0.001
	learning rate = constant
SVM	kernel = rbf
	$C = 10$
	gamma = 10

TABLE 11. Prediction results for grinding wheel grade.

Detection sensor	Prediction accuracy (%)		
	k-NN	ANN	SVM
Acoustic emission	99.4	99.5	99.7
Radial vibration	95.6	96.4	96.8
Axial vibration	98.4	98.5	98.6
Radial + axial vibration	98.4	98.5	98.6
AE + radial + axial vibration	99.8	99.8	99.9

Prediction accuracies measured in terms of F1 score.

Even after accounting for the data on fractured teeth, the prediction of the three classifiers was the most acc urate. The row005 features were not classified into other categories in the confusion matrix. Accordingly, these data did not affect prediction accuracy, which suggests that fractured teeth had no effect on the signal features of the wheel grades.

This table compares the identification accuracy using AE signals and radial/axial vibration signals on grinding wheels of various grades. Table 10 shows the respective parameters for the three classifiers. The results in Table 11 show that the AE signal was more accurate than the two vibration signals, despite having no substantial difference.

B. IDENTIFYING GRINDING WHEEL STATES

The AE signals extracted from the six grinding cycles were classified into sharp, mid, and dull conditions given the

S1 current load and images of the grinding wheel. Fifty-seven features were extracted from the AE and radial/axial vibration signals and arranged as shown in Table 12. The data were then scaled using the min-max scaler and a pipeline was established to adjust the model parameters, which were input to the three classifiers for identification. The classifier parameters are shown in Table 13.

Table 14 presents the identification results from the AE, radial vibration, and axial vibration signals. The prediction accuracy of the three classifiers was higher than 87% for both the radial and axial vibration signals, and attained 89% for the axial vibration signal when SVM was used. When the radial and axial vibration signals were combined, the prediction accuracy of k-NN and SVM increased to 90%. When the two signals were combined with the AE signal, SVM, which had
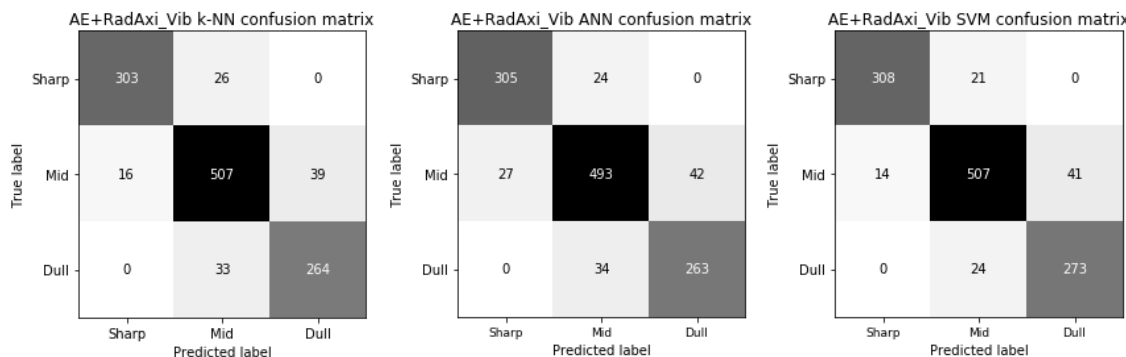
FIGURE 13. Confusion matrices for 3 wheel surface conditions for AE, radial, and axial vibration features.

TABLE 12. Data shapes from three classes.

Class	Data shape
Sharp	(1640, 57)
Mid	(2785, 57)
Dull	(1515, 57)
Total data	(5940, 57)

TABLE 13. Classifier model parameters.

Classifier	Parameter
k-NN	$K = 7$
ANN	activation function = relu
	hidden layer = [100, 100, 100]
	max iterations = 500
	alpha = 0.0001
	learning rate = constant
SVM	kernel = rbf
	$C = 10$
	gamma = 1

TABLE 14. Prediction results for wheel surface condition.

Detection sensor	Prediction accuracy (%)		
	k-NN	ANN	SVM
Acoustic emission	75.6	76.7	78.0
Radial vibration	88.3	87.0	87.4
Axial vibration	87.6	87.3	89.0
Radial + axial vibration	90.5	88.3	91.0
AE + radial + axial vibration	90.6	89.7	91.7

Prediction accuracies measured in terms of F1 score.

the most improvement, increased its accuracy only slightly to 91.7%. This suggests that the AE features did not constitute a critical factor in identifying wheel states.

Figure 13 presents the confusion matrices for the prediction results for the three groups of signal features. The matrices show that prediction errors occurred mostly in the "mid" and "dull" states. These errors were probably transition signals collected when the wheel surface transitioned to a different state because these errors occurred in nearby data. Yet, given that the wheel state underwent various transitions in a continuous grinding process and that such transition

signals, which contained features of two states, were difficult to classify, the prediction accuracy of 90% indicates that the majority of wheel states were correctly identified [46]. These identification results thus suggest that the vibration signal features are most effective in characterizing the wheel surface conditions throughout the grinding process.

VIII. CONCLUSION

In this study we develop an intelligent monitoring system based on AE and vibration signals for diamond wheel state monitoring. Empirical evidence shows that for wheels used to grind hard and brittle wafers, the key factors are the ability to self-sharpen and the surface wear/loading conditions during grinding. While analyzing signals, we originally planned to use the AE signal to monitor the state of the diamond grinding wheel. However, classifier prediction results show that monitoring multiple grinding wheel states necessitates simultaneous evaluation of multiple signals for improved discrimination [47]. Signals from other grinding recipes are collected to create more data as training samples, and the system is integrated with the grinder control system to develop a grinding wheel state assessment system.

The results are summarized as follows:

1) We propose a grinding wheel status identification system based on AE and vibration signals, which effectively identifies the grade and loading/wear of diamond grinding wheels. This system can be applied in the processing test development stage of a new grinding process (workpiece of new material, or a new grinding wheel), and provides intelligent judgments about the grinding status and helps optimize the process.

2) We use a hydrophone AE sensor to monitor the grinding wheel. Although this sensor is suitable for grinding in a two-axis rotation mode as it is not limited by the grinding type, it is rarely addressed in related studies.

3) We show that it is necessary to identify the grade of diamond wheels, because this affects the grinding efficiency and is related to wafer defects. In this work, we use five different grades of grinding wheels to establish feature samples and identification models. In the future, new grinding wheels can be used for online wheel grade detection.

4) We use the classifiers to verify the efficacy of the extracted features. The classifiers' identification results show that the AE signal yields superior performance in discriminating wheel grades and that the vibration signals better discriminate the surface conditions of the grinding wheel.

REFERENCES

[1] E. A. Dias, F. B. Pereira, S. L. M. R. Filho, and L. C. Brandão, "Monitoring of through-feed centreless grinding processes with acoustic emission signals," *Measurement*, vol. 94, pp. 71–79, Dec. 2016.

[2] P. S. Sreejith and B. K. A. Ngoi, "Material removal mechanisms in precision machining of new materials," *Int. J. Mach. Tools Manuf.*, vol. 41, no. 12, pp. 1831–1843, Sep. 2001.

[3] T. Dobrescu and F. Anghel, "Silicon wafers rotation grinding method and surface grinding on a rotary table," *Ann. Oradea Univ.*, vols. 7–17, pp. 807–813, 2008. [Online]. Available: http://imt.uoradea.ro/auo.fmte/files-2008/MECATRONICA_files/DOBRESCU%20TIBERIU%201.pdf

[4] M. P. Groover, *Introduction to Manufacturing Processes*, 1st ed. Hoboken, NJ, USA: Wiley, Oct. 2011, p. 720.

[5] J. Kundrák, V. Fedorovich, A. P. Markopoulos, I. Pyzhov, and N. Kryukova, "Diamond grinding wheels production study with the use of the finite element method," *J. Adv. Res.*, vol. 7, no. 6, pp. 1057–1064, Nov. 2016.

[6] Y. D. Filatov, "Polishing of precision surfaces of optoelectronic device elements made of glass, sitall, and optical and semiconductor crystals: A review," *J. Superhard Mater.*, vol. 42, no. 1, pp. 30–48, Jun. 2020.

[7] Z. Yang, Z. Yu, C. Xie, and Y. Huang, "Application of Hilbert–Huang transform to acoustic emission signal for burn feature extraction in surface grinding process," *Measurement*, vol. 47, pp. 14–21, Jan. 2014.

[8] T. W. Liao, "Feature extraction and selection from acoustic emission signals with an application in grinding wheel condition monitoring," *Eng. Appl. Artif. Intell.*, vol. 23, no. 1, pp. 74–84, Feb. 2010.

[9] M. S. H. Bhuiyan, I. A. Choudhury, M. Dahari, Y. Nukman, and S. Z. Dawal, "Application of acoustic emission sensor to investigate the frequency of tool wear and plastic deformation in tool condition monitoring," *Measurement*, vol. 92, pp. 208–217, Oct. 2016.

[10] W. Hundt, D. Leuenberger, F. Rehsteiner, and P. Gygax, "An approach to monitoring of the grinding process using acoustic emission (AE) technique," *CIRP Ann.*, vol. 43, no. 1, pp. 295–298, Jan. 1994.

[11] J. Webster, W. P. Dong, and R. Lindsay, "Raw acoustic emission signal analysis of grinding process," *CIRP Ann.*, vol. 45, no. 1, pp. 335–340, Jan. 1996.

[12] E. Susič and I. Grabec, "Characterization of the grinding process by acoustic emission," *Int. J. Mach. Tools Manuf.*, vol. 40, no. 2, pp. 225–238, Jan. 2000.

[13] P. R. de Aguiar and H. Thomazella, "Digital signal processing of acoustic emission signal for monitoring the dressing operation," in *Proc. 20th Int. Conf. Mech. Eng.*, Gramado, Brazil, Nov. 2009. [Online]. Available: https://www.abcm.org.br/anais/cobem/2009/pdf/COB09-1480.pdf

[14] T. W. Liao, C.-F. Ting, J. Qu, and P. J. Blau, "A wavelet-based methodology for grinding wheel condition monitoring," *Int. J. Mach. Tools Manuf.*, vol. 47, nos. 3–4, pp. 580–592, Mar. 2007.

[15] D. E. Lee, I. Hwang, C. M. O. Valente, J. F. G. Oliveira, and D. A. Dornfeld, "Precision manufacturing process monitoring with acoustic emission," *Int. J. Mach. Tools Manuf.*, vol. 46, no. 2, pp. 176–188, Feb. 2006.

[16] P. R. Aguiar, P. J. A. Serni, E. C. Bianchi, and F. R. L. Dotto, "In-process grinding monitoring by acoustic emission," in *Proc. IEEE Int. Conf. Acoust., Speech, Signal Process.*, Montreal, QC, Canada, vol. 5, May 2004, p. V-405.

[17] D. He, R. Li, J. Zhu, and M. Zade, "Data mining based full ceramic bearing fault diagnostic system using AE sensors," *IEEE Trans. Neural Netw.*, vol. 22, no. 12, pp. 2022–2031, Dec. 2011.

[18] T. W. Hwang, E. P. Whitenton, N. N. Hsu, G. V. Blessing, and C. J. Evans, "Acoustic emission monitoring of high speed grinding of silicon nitride," *Ultrasonics*, vol. 38, nos. 1–8, pp. 614–619, Mar. 2000.

[19] C.-S. Liu and Y.-A. Li, "The sensing technology of applying the acoustic emission sensor to the grinding wheel loading phenomenon," in *Proc. 14th IEEE/ASME Int. Conf. Mech. Embedded Syst. Appl. (MESA)*, Oulu, Finland, Jul. 2018, pp. 1–6.

[20] Y. P. Chang, J. J. Fang, Y. Kang, K. M. Chang, and C. C. Wang, "The diagnosis of grinding state through the combination of time-frequency analysis and statistical process control," *J. Technol.*, vol. 30, no. 1, pp. 65–72, Jun. 2015.

[21] J. Badger, S. Murphy, and G. E. O'Donnell, "Acoustic emission in dressing of grinding wheels: AE intensity, dressing energy, and quantification of dressing sharpness and increase in diamond wear-flat size," *Int. J. Mach. Tools Manuf.*, vol. 125, pp. 11–19, Feb. 2018.

[22] T. W. Liao, F. Tang, J. Qu, and P. J. Blau, "Grinding wheel condition monitoring with boosted minimum distance classifiers," *Mech. Syst. Signal Process.*, vol. 22, no. 1, pp. 217–232, Jan. 2008.

[23] A. Marec, J.-H. Thomas, and R. El Guerjouma, "Damage characterization of polymer-based composite materials: Multivariable analysis and wavelet transform for clustering acoustic emission data," *Mech. Syst. Signal Process.*, vol. 22, no. 6, pp. 1441–1464, Aug. 2008.

[24] Z. Wang, P. Willett, P. R. DeAguiar, and J. Webster, "Neural network detection of grinding burn from acoustic emission," *Int. J. Mach. Tools Manuf.*, vol. 41, no. 2, pp. 283–309, Jan. 2001.

[25] J.-S. Kwak and J.-B. Song, "Trouble diagnosis of the grinding process by using acoustic emission signals," *Int. J. Mach. Tools Manuf.*, vol. 41, no. 6, pp. 899–913, May 2001.

[26] C. H. R. Martins, P. R. Aguiar, A. Frech, and E. C. Bianchi, "Tool condition monitoring of single-point dresser using acoustic emission and neural networks models," *IEEE Trans. Instrum. Meas.*, vol. 63, no. 3, pp. 667–679, Mar. 2014.

[27] C. Lv and H. Li, "Acoustic emission signal processing of grinding monitor," in *Proc. 3rd Int. Congr. Image Signal Process.*, Yantai, China, Oct. 2010, pp. 3836–3838.

[28] *BSG-V Operation Manual*, SPEEDFAM, Hsinchu, Taiwan, 2015.

[29] D. M. S. Ribeiro, P. R. Aguiar, L. F. G. Fabiano, D. M. D'Addona, F. G. Baptista, and E. C. Bianchi, "Spectra measurements using piezoelectric diaphragms to detect burn in grinding process," *IEEE Trans. Instrum. Meas.*, vol. 66, no. 11, pp. 3052–3063, Nov. 2017.

[30] N. Ding, J. Duan, C. Liu, S. Jiang, and S. Cui, "Experimental study on the relationship between acoustic emission signal and grinding wheel wear," in *Proc. IEEE 4th Adv. Inf. Technol., Electron. Autom. Control Conf. (IAEAC)*, Chengdu, China, Dec. 2019, pp. 2699–2703.

[31] C.-S. Liu and Y.-A. Li, "Evaluation of grinding wheel loading phenomena by using acoustic emission signals," *Int. J. Adv. Manuf. Technol.*, vol. 99, nos. 5–8, pp. 1109–1117, Aug. 2018.

[32] R. Thomazella, W. N. Lopes, P. R. Aguiar, F. A. Alexandre, A. A. Fiocchi, and E. C. Bianchi, "Digital signal processing for self-vibration monitoring in grinding: A new approach based on the time-frequency analysis of vibration signals," *Measurement*, vol. 145, pp. 71–83, Oct. 2019.

[33] Y.-K. Lin, B.-F. Wu, and C.-M. Chen, "Characterization of grinding wheel condition by acoustic emission signals," in *Proc. Int. Conf. Syst. Sci. Eng. (ICSSE)*, Jun. 2018, pp. 1–6.

[34] W. Yin-Ling and L. Hua-Cong, "Research on acoustic emission source localization of carbon fiber composite plate based on wavelet neural network," in *Proc. IEEE 10th Int. Conf. Mech. Aerosp. Eng. (ICMAE)*, Brussels, Belgium, Jul. 2019.

[35] Y. K. Lin, B. F. Wu, C. M. Chen, and C. J. Ting, "Investigation on the characteristic of acoustic emission signal from different grade of grinding wheels in sapphire wafer grinding," in *Proc. 8th Int. Conf. Asian Soc. Precis. Eng. Nanotechnol.*, Matsue, Japan, Nov. 2019, p. P76.

[36] P. Lezanski, "An intelligent system for grinding wheel condition monitoring," *J. Mater. Process. Technol.*, vol. 109, no. 3, pp. 258–263, Feb. 2001.

[37] V. Ovcharuk and M. Kutsenko, "Features of spectral analysis methods application for solving problems of acoustic emission signals processing," in *Proc. 3rd Russian-Pacific Conf. Comput. Technol. Appl. (RPC)*, Vladivostok, Russia, Aug. 2018, doi: 10.1109/RPC.2018.8482221.

[38] J. S. Rad, Y. Zhang, F. Aghazadeh, and Z. C. Chen, "A study on tool wear monitoring using time-frequency transformation techniques," in *Proc. Int. Conf. Innov. Design Manuf. (ICIDM)*, Montreal, QC, Canada, Aug. 2014, doi: 10.1109/IDAM.2014.6912718.

[39] P. Shi, L. Hong, and D. He, "Using long short term memory based approaches for carbon steel fatigue remaining useful life prediction," in *Proc. Prognostics Syst. Health Manage. Conf. (PHM-Chongqing)*, Chongqing, China, Oct. 2018. [Online]. Available: https://ieeexplore.ieee.org/document/8603495, doi: 10.1109/PHM-Chongqing.2018.00187.

[40] C. M. Bishop, *Pattern Recognition and Machine Learning*. New York, NY, USA: Springer, 2007.

[41] J.-S. Kwak and M.-K. Ha, ''Neural network approach for diagnosis of grinding operation by acoustic emission and power signals,'' *J. Mater. Process. Technol.*, vol. 147, no. 1, pp. 65–71, Mar. 2004.

[42] D. M. D'Addona, S. Conte, W. N. Lopes, P. R. de Aguiar, E. C. Bianchi, and R. Teti, ''Tool condition monitoring of single-point dressing operation by digital signal processing of AE and AI,'' in *Proc. 11th CIRP Conf. Intell. Comput. Manuf. Eng.*, Gulf of Naples, Italy, Jul. 2017.

[43] N. N. An, N. Q. Thanh, and Y. Liu, ''Deep CNNs with self-attention for speaker identification,'' *IEEE Access*, vol. 7, pp. 85327–85337, 2019.

[44] D. Goyal, A. Choudhary, B. S. Pabla, and S. S. Dhami, ''Support vector machines based non-contact fault diagnosis system for bearings,'' *J. Intell. Manuf.*, vol. 31, no. 5, pp. 1275–1289, Jun. 2020.

[45] C.-H. Lee, J.-S. Jwo, H.-Y. Hsieh, and C.-S. Lin, ''An intelligent system for grinding wheel condition monitoring based on machining sound and deep learning,'' *IEEE Access*, vol. 8, pp. 58279–58289, 2020.

[46] C. Cheng, J. Li, Y. Liu, M. Nie, and W. Wang, ''Deep convolutional neural network-based in-process tool condition monitoring in abrasive belt grinding,'' *Comput. Ind.*, vol. 106, pp. 1–13, Apr. 2019.

[47] R. Huang, Y. Liao, S. Zhang, and W. Li, ''Deep decoupling convolutional neural network for intelligent compound fault diagnosis,'' *IEEE Access*, vol. 7, pp. 1848–1858, 2019.

YU-KUN LIN (Student Member, IEEE) is currently pursuing the Ph.D. degree with the Institute of Electrical and Computer Engineering, National Chiao Tung University, Hsinchu, Taiwan. He has worked with the Industry Technology Research Institute for more than eight years as an Electrical Control Engineer. His current research interests include grinding processing for hard and brittle material, signal processing, data mining, and machine learning.

BING-FEI WU (Fellow, IEEE) received the B.S. and M.S. degrees in control engineering from National Chiao Tung University (NCTU), Hsinchu, Taiwan, in 1981 and 1983, respectively, and the Ph.D. degree in electrical engineering from the University of Southern California, Los Angeles, CA, USA, in 1992.

Since 1992, he has been with the Department of Electrical and Computer Engineering, where he was promoted to a Professor in 1998 and a Chair Professor in 2020, respectively. He has been the President of the Taiwan Association of System Science and Engineering and the Director of the Control Engineering Program, Ministry of Science and Technology, Taiwan, since 2019. He served as the Director of the Institute of Electrical and Control Engineering, NCTU, in 2011. His research interests include image recognition, physiological informatics, vehicle driving safety and control, intelligent robotic systems, and intelligent transportation systems. He has received numerous research honors and awards, including the FutureTech Breakthrough Award from 2017 to 2019 and the Outstanding Research Award in 2015 and 2019, all from the Ministry of Science and Technology, Taiwan, the Technology Invention Award of Y. Z. Hsu Scientific Award from the Y. Z. Hsu Foundation in 2014, the National Invention and Creation Award of the Ministry of Economic Affairs, Taiwan, in 2012 and 2013, the Outstanding Research Award of the Pan Wen Yuan Foundation in 2012, the Best Paper Award in the 12th International Conference on ITS Telecommunications, in 2012, the Best Technology Transfer Contribution Award from the National Science Council, Taiwan, in 2012, and the Outstanding Automatic Control Engineering Award from the Chinese Automatic Control Society in 2007. He founded and was the first Chair of the Taipei Chapter of the IEEE Systems, Man and Cybernetics Society (SMCS) in 2003. He was also the Chair of the Technical Committee on Intelligent Transportation Systems with IEEE SMCS in 2011. He is currently an Associate Editor of the IEEE Transactions on Systems, Man and Cybernetics: Systems.

• • •